

Dielectronic recombination resonances in F^{6+}

M. Tokman, N. Eklöw, P. Glans,* E. Lindroth, and R. Schuch

Atomic Physics, Department of Physics, SCFAB, Stockholm University, S-106 91 Stockholm, Sweden

G. Gwinner, D. Schwalm, and A. Wolf

Max-Planck-Institut für Kernphysik, 69117 Heidelberg, Germany

A. Hoffknecht, A. Müller, and S. Schippers

Institut für Kernphysik, Strahlencentrum der Justus-Liebig-Universität, 35392 Giessen, Germany

(Received 7 December 2001; published 11 July 2002)

Electron-ion recombination spectra of the Li-like ion F^{6+} in the energy range 0.0–0.6 eV from two different ion storage rings are presented, showing excellent agreement. The experimental results are compared with a calculated spectrum, obtained by combination of relativistic many-body methods and complex rotation, and the agreement is found to be very good. The recombination spectrum in the studied energy region is determined by the $2p_j6\ell'_j$ dielectronic recombination resonances. The lowest-energy resonances are found around 10 meV, and include one broad resonance overlapping the threshold. The recombination rate coefficients are, even in this region, very well accounted for by the calculation. It is further shown that the nonrelativistically allowed resonances contribute to less than 60% of the integrated rate coefficients in the specified energy range.

DOI: 10.1103/PhysRevA.66.012703

PACS number(s): 34.80.Lx, 31.25.Jf, 32.80.Dz

I. INTRODUCTION

In electron-ion collisions, a free electron may be captured by an ion which is simultaneously excited. In an inverse Auger process a doubly excited state is created, and if this intermediate state decays radiatively, dielectronic recombination (DR) is completed. Dielectronic recombination is a fundamental recombination process important for modeling of astrophysical and fusion plasmas. In addition, it is a tool for studying the structure and decay channels of atomic doubly excited states. It gives access also to those states in ions which are not accessible through photon excitation from the ground state.

The development of ion storage rings and cooling techniques has greatly improved the accurate determination of resonance positions (at present with 1–10 meV precision for low-energy resonances) and recombination rate coefficients on an absolute scale, compared to plasma [1,2] and single-pass [3,4] experiments.

Most of the dielectronic recombination data needed in applications are calculated using so-called production codes. The storage ring experiments make it possible to benchmark calculations and to obtain a better understanding of their accuracy.

Here we present a detailed determination of recombination of lithiumlike fluorine. Lithiumlike ions are simple enough to be treated with pure *ab initio* methods due to the relatively simple structure of both the initial ion and the berylliumlike recombined ion, but still sufficiently complicated to require a full many-body treatment. To match the experimental precision achieved at present, it is necessary to ac-

count for correlation to high orders as well as for relativistic and radiative effects.

Calculations taking these effects into account have been performed and the results are compared with spectra from two independent measurements recorded at two different heavy-ion storage-rings, TSR and CRYRING. The consistency between these two measurements is also an important check for the reliability of merged-beam recombination experiments.

Some basic aspects of the recombination process are discussed in Sec. II. In Sec. III we discuss the computational method, followed by a description of the experimental work in Sec. IV. Experiment and theory are compared in Sec. V.

II. DESCRIPTION OF THE PROCESS

Dielectronic recombination is a resonant process where an electron recombines with an ion through

$$A^{q+} + e^- \rightarrow A^{(q-1)+**} \rightarrow A^{(q-1)+*} + \hbar\omega, \quad (1)$$

where $A^{(q-1)+**}$ denotes the resonant doubly excited state and $A^{(q-1)+*}$ any state bound below the ionization threshold. Relatively far from the threshold, i.e., when the energy distance from the threshold is much larger than the width of the resonance, Eq. (1) can be regarded as a two-step process. Furthermore, if there are no overlapping resonances of the same symmetry, a common situation, the cross section contribution of one doubly excited state is well described by a Lorentz profile

$$\sigma(\varepsilon_e) = \frac{1}{\pi} S \frac{\Gamma/2}{(E_d - E_{ion} - \varepsilon_e)^2 + \Gamma^2/4}, \quad (2)$$

*Present address: Department of Engineering, Physics and Mathematics, Mid-Sweden University, S-851 70 Sundsvall, Sweden.

where ε_e is the energy of the incident electron, $(E_d - E_{ion})$ is the energy position of the doubly excited state with respect to the initial state in the target ion, and Γ is the natural lifetime width of the doubly excited state. The integrated cross section, or the strength S , is proportional to the capture rate $A_{i \rightarrow d}^a$ into the doubly excited state d , and to the probability of state d to decay radiatively to a nonautoionizing level.

$$S = \int \sigma(\varepsilon_e) d\varepsilon_e = \frac{\hbar^3 \pi^2}{2m_e(E_d - E_{ion})} \frac{g_d}{g_i} \frac{A_{i \rightarrow d}^a \sum_s A_{d \rightarrow s}^{rad}}{A^a + \sum_s A_{d \rightarrow s}^{rad}}. \quad (3)$$

The multiplicity of the intermediate doubly excited state is given by g_d and that of the initial target state by g_i , with $g_i = 2$ for the Li-like F^{6+} ion. $A^a = \Gamma^a/\hbar$ is the total autoionization rate from the doubly excited state d , and $A_{d \rightarrow s}^{rad}$ is the radiative transition rate from level d to a level s below the ionization threshold, which, in the dipole approximation, is given by

$$A_{d \rightarrow s}^{rad} = \frac{1}{g_d} \sum_{M_s, M_d} \frac{e^2}{4\pi\epsilon_0} \frac{4}{3\hbar} \left(\frac{\omega}{c}\right)^3 \langle \Psi_s^{J_s M_s} | \mathbf{r} | \Psi_d^{J_d M_d} \rangle^2, \quad (4)$$

with $\omega = (E_d - E_s)/\hbar$, where E_s is the energy of a specific final state. The sum in Eq. (4) is over all magnetic substates of the two levels d and s . The last denominator in Eq. (3) equals the total transition rate Γ/\hbar from the doubly excited state. If this state, as in the case discussed here, can autoionize only to the ground state of the target ion then the autoionization rate A^a in the denominator equals the capture rate $A_{i \rightarrow d}^a$ in the nominator. As can be seen in Eq. (3), the strength is inversely proportional to the position of the resonance relative to threshold (i.e. relative to the initial state in the target ion), $(E_d - E_{ion})$, and depends crucially on the slowest type of the decay of the doubly excited state through the ratio $A^a A_{d \rightarrow s}^{rad}/(A^a + A_{d \rightarrow s}^{rad})$. For light to medium heavy systems the radiative rate is usually the slowest, and it is thus this rate that determines the recombination rate. Exceptions to this rule may occur when the two electrons are very asymmetrically excited ($n_1 \ll n_2$), but it holds for all the doubly excited states studied here.

For resonances close to threshold, perhaps with the width of the resonant state overlapping it, the just described isolated resonance approach will not be valid. The shape of the resonance is then not simply a Lorentzian but is strongly modified by the threshold. Close to the threshold the direct radiative recombination (RR) channel is also important, i.e., the system proceeds directly from the initial to the final state in Eq. (1) without the doubly excited intermediate step. When the amplitudes for radiative and dielectronic recombination are of the same order of magnitude these processes should, in principle, be treated in a unified way. Photoionization calculations are good guides for how such calculations can be performed.

Recombination is the time inverse of photoionization, and the cross section for photoionization is often calculated as

photoabsorption. This is possible because if the system, after absorbing a photon, enters into a doubly excited state above the ionization threshold, it will more or less always decay by electron emission and thus finally contribute to ionization. The probability that the system emits a photon instead and decays back to a bound state is usually very small since $A^{rad} \ll A^a$. In the same way the recombination cross section will be completely governed by photon emission when $A^{rad} \ll A^a$, since then $A^a A^{rad}/(A^a + A^{rad}) \approx A^{rad}$. Hence, recombination can be calculated as the time inverse of photoabsorption.

The calculations on recombination of F^{6+} presented here have been performed using two methods. With relativistic many-body perturbation theory in an all-order formulation we have calculated the doubly excited states and obtained resonance positions and widths. This method has previously been used for lithiumlike argon, neon, carbon, and nitrogen [5–9], and Eq. (3) was used to obtain the strength contributed by each resonance. With an alternative approach we also calculate the cross section directly as the time inverse of photoabsorption. Here no assumption is being made about the shape of the resonances and any interference between resonances or between DR and RR is automatically included. In Sec. III we first describe the general features of the calculations that both methods have in common. In Sec. III D the first method is outlined and then in Sec. III E the alternative approach is described.

III. COMPUTATIONAL METHOD

For the description of doubly excited states, an accurate treatment of correlation is generally required. Many-body perturbation theory (MBPT) is a method with a high potential for accuracy, especially in its all-order formulation. The approach used here was first implemented for bound states by Salomonson and Öster [10]. The one-particle Schrödinger Hamiltonian is discretized in a spherical box and on a radial mesh, resulting in a symmetric matrix. Diagonalization of this matrix gives a discrete basis set for each ℓ quantum number, complete on the grid chosen. In Ref. [10] the non-relativistic two-electron wave function is expanded in these basis sets and the two-electron problem is solved essentially exactly in an iterative procedure. The relativistic counterpart (RMBPT) [11] starts with the Dirac equation, neglects radiative corrections but includes all relativistic effects within the so-called no-virtual pair approximation (i.e., neglecting virtual electron-positron pairs). This procedure includes all effects to order α^2 Ry. For systems with more than two electrons, Salomonson and Öster have implemented the coupled-cluster single- and double-excitation scheme (CCSD) [12], which is an approximation to the full many-particle problem in that it neglects true three- and four- etc., particle excitations.

The CCSD approach has also been used for relativistic calculations, e.g., by Lindroth and Hvarfner [13] for berylliumlike iron and molybdenum. In Ref. [13] it is also explained how the Breit interaction, accounting for the magnetic part and the retardation of the electron-electron interaction, can be treated on equal footing with the ordinary

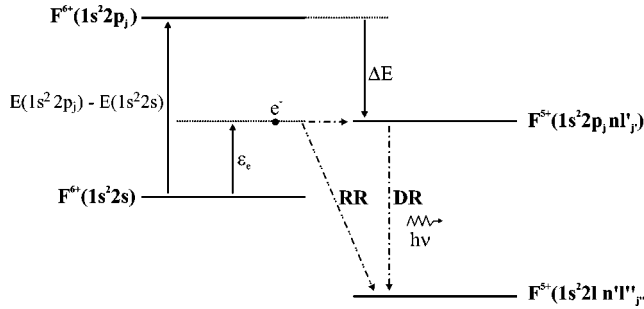


FIG. 1. An electron with a c.m. energy ϵ_e recombines resonantly with a F^{6+} ion to form a doubly excited state in F^{5+} . Note that DR is only completed if the recombined ion decays by photon emission to a state below the $F^{6+}(1s^2 2s)$ level. The solid arrows in the level diagram indicate how ϵ_e is related to the excitation energy $E(1s^2 2p_j) - E(1s^2 2s)$ of the core electron and the binding energy of the outer electron ΔE .

Coulomb interaction between the electrons. This approach is now customary and is also used in this work.

A. The lithiumlike ion

The resonances of interest here (situated up to 0.6 eV above the first ionization threshold of F^{5+}) are due to doubly excited states above the $F^{6+}(1s^2 2s)$ level, but bound below the $F^{6+}(1s^2 2p_j)$ levels. A schematic example is shown in Fig. 1. The recombination resonances are thus to be found, see Eq. (1), at relative electron energies

$$\epsilon_e = E(1s^2 2p_j) - E(1s^2 2s_{1/2}) - \Delta E, \quad (5)$$

where ΔE is the binding energy of the outer electron with respect to the excited target. From Eq. (5) it is clear that if the resonance positions are to be determined accurately it is important to calculate the $(2p_j - 2s)$ splittings very carefully. The energies of the $F^{6+}(1s^2 2\ell_j)$ states are calculated with relativistic many-body perturbation theory in an all-order formulation within the single- and double-excitation scheme described in Refs. [12,13]. The results of the calculation are presented in Sec. V A.

B. Doubly excited states in the berylliumlike ion

To calculate ΔE in Eq. (5), the interaction between the outer electron and the $1s^2$ core as well as with the inner valence electron ($2p_j$) has to be treated. The calculation of the interaction between the outer electron and the core follows that of the interaction of the $2\ell_j$ state with the core. The results are given in Sec. V B.

The autoionizing character of the states appears when the valence-valence interaction is turned on since it is responsible for the coupling to the $2s\epsilon\ell_j$ continua. This interaction is also crucial for a precise determination of the resonance positions.

To be able to describe autoionizing states, a description of the continuum of the outgoing electrons is needed. *Complex rotation* is used to be able to represent continuum wave functions in a limited cavity. The combination of many-body perturbation theory and complex rotation has earlier been used

in the nonrelativistic case [14,15] as well as in the relativistic case [5,7–9]. The method of complex rotation, where the radial coordinates in the Hamiltonian are rotated, $r \rightarrow re^{i\theta}$, has been used for a long time by many groups to account for the instability of autoionizing states, see, e.g., Refs. [16–18]. The method gives the autoionization width of the doubly excited state directly as the imaginary part of a complex energy. The real part of the energy corresponds to the position of the state.

C. Perturbation expansion from an extended model space

The resonances in the berylliumlike ion F^{5+} are in the studied energy range dominated by the configurations $2p_j 6\ell'_j$, i.e., by 22 configurations which are close in energy and which are expected to mix strongly. The mixing is in fact often complete since many states are rather well described in *LS* coupling while a relativistic calculation naturally starts with *jj*-coupled configurations. A general formulation of many-body perturbation theory which can handle degenerate or quasidegenerate *model spaces* (see below) has been developed by Lindgren [19] and has also been discussed in connection with doubly excited states [20].

The idea behind the concept of an *extended model space* is that certain strongly coupling configurations, forming the *model space*, are included through direct diagonalization of the Hamiltonian, while other configurations are included by perturbation theory. The perturbation expansion can be carried on to *all orders* and can further be assumed to converge fast if the model space is well chosen. Below we give a brief outline of the theory.

In the Rayleigh-Schrödinger perturbation formalism of Ref. [19] the starting point is the choice of a model Hamiltonian, H_0 , and a suitable model space, spanned by m eigenstates, Φ_0 , to H_0 . Different choices are possible for H_0 . A common choice is to let H_0 include the Hartree-Fock potential from the closed shell core. For the rather asymmetric states used here (one of the valence electrons is more extended than the other) it is advantageous to include also a decent approximation of the potential from the inner valence electron as felt by the outer electron. Such a potential speeds up convergence considerably and can also alleviate problems with intruder states [20]. A convenient choice is a so-called *projected potential* [20,21]. The idea is to construct a potential accounting for the dominating part of the screening of the outer electron by the inner electron while the inner electron itself sees just an unscreened core. The additional requirement that the Hermiticity of H_0 should be preserved leads to a nonlocal potential that has to be generated in an iterative procedure. The potential is nevertheless very easy to use in the perturbation expansion [21].

The model space is the subspace, spanned by a few configurations, in which an *effective Hamiltonian* is defined. The concept of an effective Hamiltonian, which is explained below, was introduced by Feshbach in the 1950s [22]. There is a considerable freedom in choosing the model space, but it is advantageous to include strongly mixing configurations. The model space for F^{5+} will then, in a conventional calculation, consist of all the 22 $2p_j 6\ell'_j$ configurations. Since parity is a

good quantum number, it is, however, possible to restrict the model space to include only configurations of one particular parity in a practical calculation.

The projection onto the model space is written as

$$P = \sum_i^m |\Phi_0^i\rangle\langle\Phi_0^i|, \quad (6)$$

where each Φ_0^i denotes a $(2p_j6\ell_j')_J$ configuration coupled to a given total angular momentum, J . Here m is the dimension of the model space and generally there are m well-defined eigenstates of the full Hamiltonian, which have their major part within the model space and satisfy the equation

$$H\Psi^a = (H_0 + V)\Psi^a = E^a\Psi^a. \quad (7)$$

The so-called ‘‘model functions’’ are given by the projection of Ψ^a onto the model space, i.e.,

$$\Psi_0^a = P\Psi^a \quad (a = 1, 2, \dots, m). \quad (8)$$

A model function is thus a superposition of configurations within the model space, i.e., in the present case a superposition of $2p_j6\ell_j'$ configurations. The model functions are chosen in such a way that they are linearly independent, and thus there is a one-to-one correspondence between the m exact solutions and the model functions. It is then possible to define a single *wave operator* Ω , which transforms all the model functions back to the exact ones,

$$\Psi^a = \Omega\Psi_0^a \quad (a = 1, 2, \dots, m). \quad (9)$$

The wave operator satisfies a generalized Bloch equation [19,23]. Armed with Ω and P it is possible to obtain an expression for the effective Hamiltonian H_{eff} , which generates the exact eigenvalues when operating on the model functions,

$$H_{\text{eff}}\Psi_0^a = E^a\Psi_0^a \quad (a = 1, 2, \dots, m). \quad (10)$$

The model functions can be found by diagonalization of the effective Hamiltonian within the model space. In zeroth order the effective Hamiltonian H_{eff} is identical to $H = H_0 + V$. In higher orders the effects from configurations outside the model space will modify the effective Hamiltonian and as a consequence the admixture of the configurations in the model functions Ψ_0 will change slightly. A successively better approximation to Ω as well as to the functions Ψ^a is generated in every iteration. The convergence is generally fast when all strongly interacting configurations are included in the model space. We notice though that it sometimes is possible to obtain the effective Hamiltonian using a nonperturbative procedure [24].

The effective Hamiltonian in the described procedure will not have the form of a *symmetric* matrix and, hence, it will not be Hermitian. As long as the perturbation expansion converges, this is not a problem. The functions $\Psi^a = \Omega\Psi_0^a$ are eigenstates to the Hermitian Hamiltonian H and will be orthogonal to each other. In the case of a complex rotated Hamiltonian the matrix is not Hermitian, but complex sym-

metric. Nevertheless, even in this case the eigenfunctions can be shown to be strictly orthogonal.

D. Method 1

To obtain precise energies and widths we use the conventional extended model space approach as described in Sec. III C. The model space then consists of all $2p_j6\ell_j'$ configurations of the same parity. Most of the doubly excited states are calculated to fall in the energy range from the ionization threshold up to around 0.6 eV above threshold. The states dominated by $2p_j6s_{1/2}$ configurations as well as many states dominated by $2p_j6p_j'$ configurations are however found below threshold and are thus true bound states. These states are not necessarily well described numerically since they may be close in energy to Rydberg states converging to the $F^{6+}(1s^22s)$ threshold, i.e., of the type $2sn\ell_j$ with high n -quantum numbers. Such Rydberg states are too extended to be unaffected by the radial box used in the calculation and will not appear as physical states. The $2p_j6\ell_j'$ states that are close in energy to a Rydberg state will be affected by it and if the latter state is affected by the box description this will to some extent also be the case for the former states. This problem is, in practice, hard to avoid since the density of Rydberg states becomes very large just below the threshold and any box size will limit the number of physical Rydberg states described. The radial overlap with a localized $2p_j6\ell_j'$ state is, of course, very small, but when energies nearly coincide the admixture could anyhow be substantial. Since the Rydberg states are not calculated explicitly, their major weight is outside the model space, and it is difficult to check to which degree this is happening. In this respect it would be an advantage to use a method that yields also the Rydberg states explicitly. This is one reason to use ‘‘Method 2’’ below.

Two states, $(2p_{3/2}6p_{1/2})_{J=1}$ and $(2p_{3/2}6p_{1/2})_{J=2}$, are situated around 10 meV above threshold. The latter is very narrow while the first is broad and overlapping the threshold. Equation (3) is not well suited for resonances close above the ionization threshold, especially not if the resonance is overlapping the threshold. The implicit assumption in Eq. (3) is that the cross section has a Lorentzian shape. However, close to the threshold the cross section changes drastically. The need to calculate the energy dependence of the cross section in this region is a second reason for ‘‘Method 2’’ below.

E. Method 2

As discussed above, the most important type of configuration interaction is that within the $2p_j6\ell_j'$ configurations. To obtain the widths, it is also necessary to fully include the channels from the discretized description of the $2s_{1/2}\varepsilon\ell_j$ continua. All other configurations have only minor weight in the resonances closely above the F^{6+} threshold. A consequence of using a discretized continuum is that there is no clear distinction between it and the Rydberg states $2s_{1/2}n\ell_j$. The $2s_{1/2}n\ell_j$ states with low n are physical states that are well described in the radial box, but with increasing energy

the states transform smoothly to “box” states, which are nonphysical states able to span the true state within the limited cavity.

In “Method 2” all the configurations $2s_{1/2}n\ell_j$ (i.e., including the discretized continua) are added to the $2p_j6\ell'_j$ configurations to form a giant model space. Typically the model space now consists of several hundred configurations. The configurations outside the model space are still included by a perturbation expansion.

The extended model space method described in Sec. III C can, in principle, also be used to all orders with very large model spaces, the requirements on disk space and computing time will however give a limit beyond which such a calculation is not feasible. However, the most important contributions are now included in the model space, and thus will be treated exactly by diagonalization of the Hamiltonian and only configurations with a minor weight are included through the perturbation expansion. We have then chosen to restrict the expansion to second order in the electron-electron interaction.

A description of the $2s\epsilon\ell_j$ continua is now available. In the time inverse process, photoionization, these continua are conveniently used to span the space available for the system after photoabsorption [25], and here they are used to calculate the direct radiative recombination.

Rescigno and McKoy [26] have discussed how the method of complex rotation can be applied to photoabsorption. The cross section for absorption when the system is in bound state s is calculated as

$$\sigma_{s \rightarrow all}^{ph}(\omega) = \frac{1}{g_s} \frac{e^2}{4\pi\epsilon_0} \frac{4\pi}{3} \frac{\omega}{c} \times \text{Im} \left(\sum_n \frac{\langle \Psi_s | \mathbf{r} e^{i\theta} | \Psi_n \rangle \langle \Psi_n | \mathbf{r} e^{i\theta} | \Psi_s \rangle}{E_n - E_s - \hbar\omega} \right). \quad (11)$$

As in Eq. (4) it is assumed in Eq. (11) that the sum runs over all magnetic substates, and the result is then averaged over the magnetic substates of the initial state s by division with g_s , the multiplicity of state s . The sum over n runs over all states, the doubly excited states as well as those which represent the continua. The energy E_n is, in general, complex, and for the doubly excited states the imaginary part equals the half-width, $E_n = E_d - i\Gamma/2$. As discussed in Sec. II the absorption cross section for photons energetic enough to bring the system above the ionization threshold approximates well the photoionization cross section since the autoionization rate is much larger than the radiative rate for nearly all doubly excited states.

Equation (11) can be used in the case of recombination after a few changes. To account for electron scattering instead of photon scattering, the expression is scaled with $(k_{ph}/k_e)^2 = \hbar^2\omega^2/2m_e\epsilon_e c^2$. In order to average over the magnetic substates of the true initial state (an ion in its ground state and one free electron with multiplicity g_i) and to sum over all possible intermediate and final magnetic substates, a factor g_s/g_i is introduced. The cross section should

further be given as a function of the electron energy and according to Eq. (1) $\hbar\omega$ can be replaced with

$$\hbar\omega = \epsilon_e + E_{ion} - E_s. \quad (12)$$

With these changes Eq. (11) is transformed to

$$\sigma_s^{Recomb.}(\epsilon_e) = \frac{1}{g_i} \frac{e^2}{4\pi\epsilon_0} \frac{4\pi}{3} \frac{\omega}{c} \left(\frac{\hbar\omega}{c} \right)^2 \frac{1}{2m_e\epsilon_e} \times \text{Im} \left(\sum_n \frac{\langle \Psi_s | \mathbf{r} e^{i\theta} | \Psi_n \rangle \langle \Psi_n | \mathbf{r} e^{i\theta} | \Psi_s \rangle}{E_n - E_{ion} - \epsilon_e} \right). \quad (13)$$

The sum over n runs over all states, the doubly excited states as well as those which represent the continua. In this way both recombination through resonances as well as through direct radiative recombination are included. Equation (13) gives the cross section for recombination into a specific bound state s . The total cross section for field-free conditions can be obtained after summation over all bound states s . In storage ring experiments the motional electric fields in the magnets will result in field ionization of weakly bound states (see Sec. IV), and thus not all recombined ions are detected. To describe this the sum over s has to be truncated appropriately.

Note that the contribution from a specific term in the sum in Eq. (13) may very well be in the form of a Lorentz profile. This will be the case for a doubly excited state n , with $E_n = E_d - i\Gamma/2$, when the matrix element in Eq. (13) has a vanishingly small imaginary part. An integration over ϵ_e will then reproduce Eq. (3) with $A^a A^{rad}/(A^a + A^{rad})$ replaced by A^{rad} . When the imaginary part of the matrix element is comparable in size to the real part the cross section profile will instead be asymmetric and this would be a sign of interference between radiative recombination and dielectronic recombination.

IV. EXPERIMENT

The work presented in this paper demonstrates that the theory of dielectronic recombination of light Li-like ions has reached an accuracy that mandates comparison with experimental data of the highest achievable quality currently. While the precision of the calculations is expected to be comparable over a wide range of light Li-like ions [5,7–9], the attainable experimental spectral resolution and absolute energy calibration depend very much on the appropriate choice of ion. In the type of merged-beam experiments currently used to study electron-ion recombination, the precision of the experimental data is superior if the spectral features under consideration are located at low electron-ion collision energies. Only below ≈ 1 eV is it possible to observe detailed fine structure and finite natural linewidths. The reason for this behavior is outlined below. Dielectronic recombination resonances at such low collision energies appear if the excitation of the core, in this case $1s^2 2s_{1/2} \rightarrow 1s^2 2p_j$, requires an energy $E_{2s \rightarrow 2p} = E(1s^2 2p_j) - E(1s^2 2s_{1/2})$ corresponding very closely to the binding en-

TABLE I. The contributions to the energies for the $2s_{1/2}$, $2p_{1/2}$, and $2p_{3/2}$ states in F^{6+} , given relative to the ionization threshold, and to the $2p_{j-2s_{1/2}}$ splittings in F^{6+} .

	$2s_{1/2}$ (a.u.)	$2p_{1/2}$ (a.u.)	$2p_{3/2}$ (a.u.)	$2p_{1/2}-2s_{1/2}$ (eV) ^a	$2p_{3/2}-2s_{1/2}$ (eV) ^a
Dirac-Fock ^b	-6.801084	-6.284988	-6.280043	14.0433	14.1778
Δ Dirac-Fock-Breit ^b	0.000605	0.001024	0.000445	0.0114	-0.0045
Mass polarization		-0.000113	-0.000112	-0.0031	-0.0031
Correlation corrections (Coul.+ Br.)					
Second-order core-valence					
$\ell_{max} = 12$	-0.007162	-0.010470	-0.010392		
$\ell_{max} = 13$	-0.007162	-0.010471	-0.010393		
$\ell_{max} = 14$	-0.007163	-0.010472	-0.010394		
$\ell_{max} = 15$	-0.007163	-0.010473	-0.010395		
Extrapolation	-0.007168	-0.010483	-0.010405		
Second-order core core	0.001841	0.000835	0.000825		
Sum of all second-order correlation	-0.005327	-0.009648	-0.009581	-0.1176	-0.1157
Higher-order correlation	-0.000233	-0.000408	-0.000406	-0.0048	-0.0047
Total RMBPT	-6.806039	-6.294133	-6.289698	13.9293	14.0500
Johnson <i>et al.</i> [37] ^c				13.9284	14.0491
Radiative corrections, H-like ^d	0.000496	-0.000012	0.000013	-0.0138	-0.0131
Screening of radiative corrections ^e	-0.000155	0.000004	-0.000004	0.0044	0.0041
Total	-6.805698	-6.294141	-6.289689	13.9198	14.0409
Experiment ^f				13.9185 ± 0.0003	14.0395 ± 0.0003

^a1 a.u. = $27.211396M/(M+m_e)$ eV.

^bA Fermi distribution for the nuclear charge is used.

^cIn [37] the partial wave expansion was extended up to $\ell_{max} = 8$.

^dJohnson and Soff [38].

^eEstimated by Z^3 -scaling from Blundell [39].

^fNIST database [40]. The error estimate is found in the original reference, Palenius, H. P., Univ. of Lund (Sweden) Rep. (1971).

ergy of a Rydberg state n (see Fig. 1). For a first survey, the binding energy ΔE of this Rydberg state can be approximated by

$$\Delta E = \frac{RZ_{\text{eff}}^2}{n^2}, \quad (14)$$

where R is the Rydberg constant, $Z_{\text{eff}} = Z - 3$ is the effective charge of the Li-like ion core, and n is the principal quantum number. In F^{6+} we have the fortuitous case of $E_{2s \rightarrow 2p} \approx 14.0$ eV (see, e.g., Table I) and a binding energy of 1 Ry or 13.6 eV for the $n=6$ state. Therefore $1s^2 2s(^2S) + e^- \rightarrow 1s^2 2p(^2P) 6\ell$ DR resonances are expected to be located around 0.4 eV. Indeed, our calculations and the experiment show that the $n=6$ DR resonances, which are above threshold, are distributed between 7 and 520 meV. Resonances appearing at such low energies make Li-like fluorine a very favorable system, and the best case so far, for a detailed comparison between experiment and theory.

The recombination measurements with F^{6+} were carried out at the heavy-ion storage-ring TSR of the Max-Planck-Institut für Kernphysik in Heidelberg and at the CRYRING facility of the Manne-Siegbahn Laboratory in Stockholm.

A. TSR Experiment

In the Heidelberg experiment, a 3.9-MeV/u F^{6+} beam from the MPIK tandem accelerator was injected into the stor-

age ring using the techniques of multiturn injection and electron-cool stacking [27]. Using these methods, up to 1 mA of (electric) beam current could be stored in the ring; however, in order to minimize the influence of intrabeam scattering on the velocity spread of the ion beam, and therefore on the energy resolution of the measurement, the recombination spectra were recorded with 10–20 μA of stored beam current. Once the ion beam is injected, it is cooled by merging it with a magnetically guided, cold electron beam (density $\approx 10^7 \text{ cm}^{-3}$, longitudinal magnetic field ≈ 40 mT) over a distance of ≈ 1.5 m. Electron cooling results in a narrow (≈ 1 mm diameter) ion beam of low velocity spread ($\Delta p/p \approx 2 \times 10^{-4}$). In recombination experiments, the cooler device has a second function as an electron target. By shifting the electron velocity with respect to the speed of the ions, a desired center-of-mass (c.m.) collision energy can be realized between them. Ions that capture an electron in the cooler are detected at the next bending magnet where they leave the closed orbit of the ring due to their reduced charge. The high kinetic energy of 74 MeV makes efficient detection ($>95\%$) of single recombined ions in a scintillator-counter straightforward (see Fig. 2) [28].

The velocity spreads of the electrons and ions both lead to a broadening of the measured DR resonances. Due to the longitudinal acceleration and the adiabatic magnetic expansion of the electron beam [29,30], the longitudinal and transverse spreads of the relative electron-ion velocities are sig-

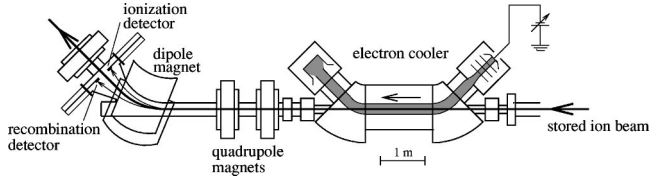


FIG. 2. The electron-cooler section of the TSR storage ring. In the dipole magnet, the recombined ions are spatially separated from the original beam and detected by a scintillator counter.

nificantly reduced and correspond in our experiment to $kT_{\parallel} \approx 0.09$ meV and $kT_{\perp} \approx 5$ meV, respectively. The temperatures have been measured *in situ*, using line-shape analysis of the relatively isolated, narrow DR resonance at $\varepsilon_e = 10$ meV (see, e.g., Fig. 4 and [31]). The transverse spread of collision energies broadens DR resonances by roughly $\ln(2) kT_{\perp}$, independent of the relative electron-ion energy. On the other hand, in the longitudinal direction the broadening scales with the collision energy as $4\sqrt{\ln(2)\varepsilon_e kT_{\parallel}}$ (full width at half-maximum). Therefore the spectral resolution is the highest at low energies and roughly equal to kT_{\perp} for collision energies

$$\varepsilon_e \lesssim \frac{\ln(2)(kT_{\perp})^2}{16kT_{\parallel}}, \quad (15)$$

where the right-hand side corresponds to ≈ 15 meV in our case.

In addition, the absolute calibration of the energy scale is important. Experimentally, the nominal collision energy in the electron-ion c.m. system, ε_e , is computed from the laboratory electron energy E_e and the ion energy E_i , which in turn is determined by E_e at cooling. E_e is obtained by measuring the cathode voltage of the electron gun and applying a space-charge correction, stemming from the fact that the small ion beam (diameter $\approx 1-2$ mm) travels in the center of a larger (48 mm diameter) electron beam. This correction is calculated and depends on the knowledge of the electron density and its distribution across the beam. Various checks have confirmed that the use of a homogeneous density is appropriate. A notable feature of merged beam experiments is that each electron-ion collision energy can be achieved for two different laboratory energies E_e , with the electron being faster or slower than the ion. If the relative collision energy is plotted along the negative-energy axis for the latter case, two mirror-symmetric spectra are obtained around $E=0$, as shown in Fig. 3. Radiative recombination has a continuous spectrum strongly peaking at $\varepsilon_e=0$ ($\sigma_{RR} \propto 1/\varepsilon_e$) and its maximum accurately labels the origin of the c.m. energy scale, independent of technical details such as space-charge corrections. Hence the knowledge of the absolute energy scale is again best at low energies. Uncertainties in the determination of E_e predominantly result in a stretching of the scale around $\varepsilon_e=0$. The measurement procedure in the TSR experiment involves a toggling of the cathode voltage at the millisecond level, as explained below. The settling time of the power supply after these jumps leads to a discrepancy between the nominal and actual cathode voltages in the mea-

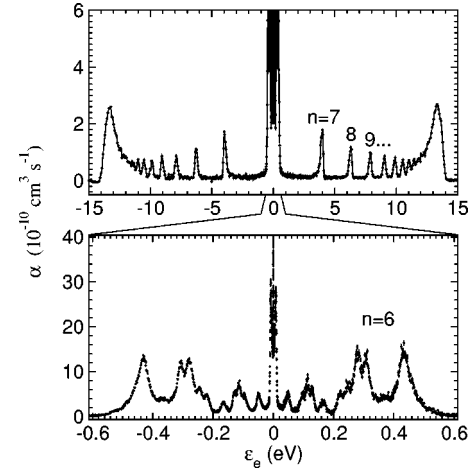


FIG. 3. TSR overview spectrum of F^{6+} , negative collision energies label data taken with $v_e < v_i$. The upper graph shows the $1s^2 2s + e^- \rightarrow 1s^2 2pn\ell$ series, with $n=6, 7, \dots$. The lower plot gives an expanded view of the $n=6$ resonances close to threshold. The narrow peak at $\varepsilon_e=0$ is due to radiative recombination and is off-scale.

surement window, leading to a stretching of the relative electron-ion energy scale that was determined to be about 2.75% by comparison with the known series limits [32]. In all TSR data plots a correction for this effect is applied. After this adjustment, the absolute accuracy of the relative energy is estimated to be $\delta\varepsilon_e/\varepsilon_e \lesssim 1\%$, but not less than 1 meV.

The Coulomb interaction between the electrons and the ions results in a drag force that pulls the ion beam towards the velocity of the electrons whenever $E_e \neq E_i$, ultimately smearing out the recombination spectrum. This problem is circumvented using a scheme where the velocity of the electron beam is cycled between a longer cooling period (30 ms) during which the electron beam is cooling the ions and a much shorter measurement window (3 ms) in which the electron beam is shifted to a velocity corresponding to a desired collision energy. It has been verified that the velocity drag on the ions can be neglected during the measurement period, as the variation of the electron density by one order of magnitude leads to line shifts of less than 0.5 meV for the narrow resonance at 10 meV.

The experimentally measured recombination rate $R(\varepsilon_e)$ is then converted into a recombination rate coefficient $\alpha(\varepsilon_e)$ which represents the electron-ion recombination rate per ion and unit electron density. The conversion procedure is described in detail in [33].

In the toroidal sections of the cooler, where the electrons and ions are merged and demerged, the c.m. collision energy is shifted and position dependent. As the field geometry is well known, a correction can be applied [34]. This step yields the final experimental recombination rate coefficient $\alpha(\varepsilon_e)$. The absolute accuracy of the rate coefficient is conservatively estimated to be $\delta\alpha/\alpha \lesssim 20\%$, it is mainly limited by the uncertainty in the number of stored ions in the ring and in the electron density. The experimental $\alpha(\varepsilon_e)$ is now compared to the theoretically computed one. The theoretical spectrum is obtained by a folding of the calculated cross-

section spectrum with the appropriate energy distribution. The theoretically computed recombination rate coefficient has to be adjusted for the fact that not all recombined ions end up in the scintillator counter. On the way from the recombination zone to the detector, the ions see motional electric fields in the magnets, especially in the dipole magnet, resulting in field ionization of ions that have recombined into sufficiently high Rydberg states. In this study, the DR signal is not affected at all by this effect, since the $n=6$ state is well below the cutoff for field ionization ($n_{\text{cut}} \approx 32$). However, radiative recombination can occur in arbitrary n at all energies ε_e . Therefore, the contribution from RR has to be cut off to describe the experimental situation. Since RR makes a small contribution for all but the smallest collision energies, this correction is not critical.

B. CRYRING experiment

The Stockholm experiment is in many ways similar to the Heidelberg experiment described above, however, there are some important differences. The most significant difference is in the way the cathode voltage is varied during the measurements: In Heidelberg fast jumps of the voltage and short measurement windows are used to avoid drag force effects, whereas in Stockholm the voltage is varied slowly in a zigzag pattern and the resulting variation of the ion velocity, caused by the drag force, is accounted for in the data analysis. Below a brief outline of the Stockholm experiment is given, more detailed descriptions of the measurement and analysis procedures have been given previously [6,9].

The F^{6+} ions were produced in an electron-beam ion source (CRYSIS) and injected into the storage ring (CRYRING) after preacceleration by a radio-frequency quadrupole accelerator to the injection energy of 300 keV/ u . After injection the ions were accelerated to their final energy of 7.8 MeV/ u by a radio-frequency acceleration system in the ring. The beam current, after the final acceleration, was typically 1–2 μ A. The ion-beam current decayed slowly with a measured mean lifetime of 36 s.

After each injection, the accelerated ion beam was cooled by a magnetically guided, cold electron beam for about 3 s before the measurement began. The two beams were collinear in the cooler over a distance of about 80 cm. In this merged region the electron beam had a diameter of 4 cm and was guided by a longitudinal magnetic field of 30 mT. The electron current was 76 mA.

During the ≈ 4 -s-long measurement window the cathode voltage was varied in a zigzag pattern. From cooling, the voltage was first monotonically increased for about 1 s to a maximum voltage, then decreased for 2 s to a minimum voltage, and finally during the last second increased back to the cooling voltage value. This zigzag scan leads to four spectral parts covering the same c.m. energy region. During the first 2 s of the scan the electrons are faster than the ions while during the last 2 s the electrons are slower than the ions. The maximum and minimum voltages were chosen so that all four spectral parts covered c.m. energies up to about 15 eV. This means that besides the $2p\ell$ resonances also all $2pn\ell$ resonances with $n > 6$ were recorded since the energy posi-

tions of the $2p\ell_j$ series limits equal the $E_{2s_{1/2} \rightarrow 2p_j}$ core excitation energies of ≈ 14.0 eV. However, note that the intensity for resonances with $n > n_{\text{cut}}$ are severely quenched due to field ionization ($n_{\text{cut}} = 22$).

After each measurement cycle the ion beam is dumped and a new injection is made. A recombination spectrum is obtained after the detected events from many identical measurement cycles have been added together. The spectrum presented from the Stockholm experiment in this work consisted of the events from 1098 cycles.

The recombined ions were detected by a surface-barrier detector positioned behind the first dipole magnet downstream from the electron cooler. The detector had a 100% detector efficiency, however, not all recombination events were recorded due to the high count rate (> 1 kHz at low c.m. energies) and the long dead time (175 μ s) of the data acquisition system that was used. The measured recombination rates were corrected for the effects of dead time in the data analysis.

The data analysis aims at obtaining absolute rate coefficients as a function of c.m. energy. Space-charge and drag-force corrections are made in the analysis in order to obtain an accurate absolute energy scale. The corrections contain a few free parameters, which are optimized to achieve as good overlap as possible between the four spectral parts from the zigzag scan. The energy scale obtained in this way is typically correct to within about 4%. If the energy of at least one feature in the spectrum is known it is possible to improve the accuracy of the energy scale significantly by a linear stretch or compression of the energy scale (since the errors in the c.m. energies typically scale close to linear with energy) so that the energy position of the feature fits the known value. In this case we used the positions of the series limits to calibrate the energy scale. The series limits do not give a very well-defined feature in the spectrum, however, their positions can easily be estimated with an accuracy better than 1%, thus the calibration gives a slight improvement of the energy scale.

Absolute rate coefficients are calculated from the measured recombination rates in a similar way as for the Heidelberg data. One difference is that the same background is assumed for all data points. The background due to electron capture in collisions with residual gas is assumed to be independent of the cathode voltage (and hence independent of the c.m. energy) and it is estimated from the measured rates at energies above the series limits, where the recombination rate is negligible compared to the background.

An expansion factor $\zeta = 100$, see Ref. [29] was used in the Stockholm experiment. This expansion factor should ideally yield $kT_{\perp e} \approx 1$ meV. However, line-shape analysis gives $kT_{\perp} = 3.0$ meV and $kT_{\parallel} = 0.10$ meV. The same values were obtained also in an earlier measurement on F^{6+} [35]. The reason for the discrepancy between the measured and the expected values of kT_{\perp} is not yet known. In addition, there are some indications of a somewhat lower measured value for kT_{\perp} , closer to the expected value of about 1 meV, from an experiment on Pb^{53+} [36].

TABLE II. A list of the different contributions to the calculated energy positions of some of the low-energy $F^{5+}(2p_j6\ell_{j'})$ resonances. Energies are given in eV.

	$2p_{3/2}6p_{1/2}$	$2p_{1/2}6d_{3/2}$	$2p_{1/2}6d_{5/2}$
	$J=1$	$J=2$	$J=3$
$(2p_j-2s_{1/2})^a +$			
Dirac-Fock description of $6\ell_{j'}$	0.0104	0.0198	0.1238
Δ Dirac-Fock-Breit for $6\ell_{j'}$	0.0006	0.0005	0.0000
polarization of $1s^2$ by $6\ell_{j'}$	-0.0072	-0.0071	-0.0019
$2p_j6\ell_{j'}$ correlation	0.0030	-0.0017	-0.0228
Total	0.0069	0.0114	0.0990

^aThe $2p_j-2s_{1/2}$ splittings include correlation and radiative corrections as listed in Table I.

V. RESULTS

A. Calculation of the lithiumlike ion

The knowledge of the $(2p_j-2s)$ splittings is essential to accurately determine the positions of the dielectronic recombination resonances. In Table I the different contributions to the $F^{6+}(2s_{1/2})$, $F^{6+}(2p_{1/2})$, and $F^{6+}(2p_{3/2})$ energies are listed. The first row lists the Dirac-Fock contribution. The second row gives the differences obtained when the Breit interaction is added to the Hamiltonian to form the Dirac-Fock-Breit Hamiltonian. The Breit interaction accounts for the magnetic part of the electron-electron interaction and for the retardation of the electromagnetic field in the low-energy limit. The retardation beyond the Breit interaction is in lowest order calculated to be only 1.6×10^{-7} a.u., -1.9×10^{-7} a.u., and -1.4×10^{-6} a.u. for $2s$, $2p_{1/2}$, and $2p_{3/2}$, respectively, and is not included in Table I. The RMBPT calculations were done with a Dirac-Fock-Breit basis set constructed in the potential from a Fermi distribution of the nuclear charge. The dominating correlation contribution comes in second order of the perturbation expansion. Table I shows the sum of the Coulomb (two order in the Coulomb interaction) and Breit interactions (one order in Coulomb and one in the Breit-interaction). The latter part gives less than 2% of the sum. The partial-wave expansion for the interaction between the valence electron and the core (core-valence correlation) is extended up to $\ell_{max}=15$. The contributions from higher angular momenta were estimated by extrapolation as shown in Table I. The contribution to the binding energy of the last electron that comes from interactions within the core (core-core correlation) is nearly one order of magnitude smaller and includes only a finite sum over partial waves. Higher-order correlation is calculated within the coupled-cluster single- and double-excitation scheme [12].

As demonstrated in Table I the RMBPT calculation is in good agreement with an earlier calculation by Johnson *et al.* [37]. The differences of 0.9 meV for both the $(2p_{1/2}-2s)$ and the $(2p_{3/2}-2s)$ splittings are dominated by the difference in second-order correlation energy and arise from the use of either a Dirac-Fock-Breit basis set to evaluate the correlation energy (present work) or a Dirac-Fock basis set (Ref. [37]). The partial-wave expansion is here carried on until $\ell_{max}=15$ and extrapolated from there. In Ref. [37] it is carried on to $\ell_{max}=8$ and then extrapolated, which also yields a small

difference. Finally, Ref. [37] includes Coulomb correlation up to third order while the present calculation includes higher-order correlation. This gives differences in the binding energies of the $2l_j$ states around 20–30 meV, but the dominating parts of these differences cancel in the $(2p_j-2s)$ splittings.

The largest radiative corrections (entering with a quantum-electrodynamical description of the ion), self-energy and vacuum polarization, have been calculated for H-like systems by Johnson and Soff [38] and for many Li-like systems by Blundell [39]. The difference between the Li- and H-like systems, often referred to as screening, is here estimated by a Z^3 scaling from the calculation on Li-like neon in Ref. [39]. This estimate should be correct to within 10%, but this uncertainty is of minor importance since the whole screening correction is only 0.004 eV for the $(2p_j-2s)$ splittings.

B. Resonances in the Be-like ion

The position of a $(2p_j6\ell_{j'})$ resonance is determined by the $(2p_j-2s)$ splittings and by the interaction of the outer electron with the $1s^2$ core as well as with the inner valence electron ($2p_j$). In Table II the different contributions to the resonance positions are listed for a few of the low energy resonances.

As a first approximation the $6l_j$ states are calculated in the potential from the core and from an electron in $n=2$, the latter is the so-called projected potential discussed in Sec. III C. The $6s$ electron has then a binding energy of ≈ 14.56 eV. Since the $(2p_{1/2}-2s)$ and $(2p_{3/2}-2s)$ splittings are 13.92 eV and 14.04 eV, respectively, the $(2p_j6s_{1/2})$ state is expected to be bound below the ionization threshold. The $6p_{1/2}$ electron has, however, a binding energy of ≈ 14.07 eV, i.e., just slightly larger in magnitude than the $(2p_{3/2}-2s)$ splitting. Thus, in this lowest order approximation the $(2p_j6p_{1/2})$ states should be slightly bound, but the following refinements were clearly necessary to sort out whether this is really the case.

First, Be-like fluorine is not well described by jj coupling. The jj configurations given in Table II are thus just rough labels indicating the most important configuration; e.g., the first $J=1$ resonance, listed in Table II as $(2p_{3/2}6p_{1/2})$, is to only 88% described by that configuration. The following $J=2$ resonance is listed as coming from the

same configuration, but is in reality dominated by $(2p_{3/2}6p_{1/2})$ and $(2p_{3/2}6p_{3/2})$ in nearly equal amounts. In this situation a reasonable first approximation can only be obtained by diagonalization of the Hamiltonian within the space of the $(2p_j6p_{j'})$ configurations. The first row in Table II gives the result of such a diagonalization when the $6l_j$ states are interacting with the core through a Dirac-Fock potential. The second row gives the difference when it interacts through a Dirac-Fock-Breit potential. For $6l_j$ states with $\ell \geq 2$ this has no effect in the figures shown. The third row gives the extra binding due to the polarization of the core by the $6l_j$ electron. This is, in principle, a correlation effect. In this approximation one finds that of the ten $(2p_j6p_{j'})_J$ states six are bound and four form resonances. The two $(2p_j6p_{j'})_J$ resonances with the lowest energy are listed in the first two columns of Table II. In the next step the interaction between the $6l_j$ and the $2p_{j'}$ electrons has to be treated more carefully. In the lowest-order approximation the interaction is just described by the so-called projected potential from an electron in $n=2$, see Sec. III C. On the fourth row of the table this description is replaced by the fully correlated description calculated as described in Sec. III D. Both Coulomb and Breit correlations are accounted for, but the latter is of minor importance.

One of the reasons to calculate the DR resonances also with Method 2 was the risk that the low-energy resonances could be affected by bound states poorly described in the radial box used in the calculation, see Sec. III D. It is then reassuring to find that the two methods give only small differences in the energy positions: 0.57, 0.73, 0.75, and 1.2 meV, respectively, for the four resonances listed in Table II. Even the width of the broad resonance at ≈ 7 meV changes only from 0.0258 eV to 0.0271 eV.

In Table III we summarize calculated resonance positions, widths, decay rates, and strengths for all doubly excited states dominated by $(2p_j6l_{j'})$ configurations above the first ionization threshold of F^{5+} . Resonance positions and widths were calculated using both method 1 (Sec. III D) and method 2 (Sec. III E), which gave similar results. In Table III those results obtained using method 1, based on fully correlated wave functions, are listed. Each state is labeled by a configuration showing the dominating contribution. This label should not be taken too seriously, since for many states several dominating configurations contribute with similar weight and the doubly excited states of F^{5+} cannot be well described by neither *LS* coupling nor *jj* coupling.

To illustrate this, the dominating *LS* term and its weight are shown in the second column of Table III. It can be noted that the two lowest-energy resonances are predominantly of $^3P^e$ symmetry and would thus not be allowed to autoionize in a pure nonrelativistic description. Then no recombination could occur through them either. In reality, however, they dominate the recombination spectrum close to the ionization threshold. The third fine-structure level of $^3P^e$, on the other hand, is bound below the ionization threshold.

There are three $2p6\ell$ levels, situated above the ionization threshold, listed in the ‘‘Atomic Spectra Database’’ provided by NIST [40]. These levels denoted below as level 1, level 2,

and level 3 are identified as $2p6p\ ^1D_2$, $2p6d\ ^3D^o$, and $2p6d\ ^1F_3^o$, respectively, and they are listed at energies of 0.1178, 0.2623, and 0.4756 eV above the threshold. We expect our calculated resonance positions to be good within a few meV. This estimate is supported by the agreement with the experimental data, see Sec. V C. If we compare the resonance positions from Table III with the literature values we find a good agreement for the first one of the three levels in the literature but poor agreement for the other two levels.

Our calculated value for the $2p6p\ ^1D_2$ level is 0.1158 eV, which only differs by 2 meV from the literature value for level 1. For the three $2p6d\ ^3D^o$ levels, on the other hand, the calculated positions are 0.2240, 0.2471, and 0.4706 eV, and neither of those values is close to the literature value of 0.2623 eV for level 2. In fact, there is only one level in Table III with an energy close to that literature value, the $2p6f\ ^3G_3$ level at 0.2628 eV. However, level 2 has odd parity while the $2p6f\ ^3G_3$ level has even parity. Since parity is a good quantum number the two levels in question cannot be the same. We therefore conclude that the database value for level 2 must be wrong. The incorrect value in the literature is most likely due to the wrong assignment for one of the lines in the photon spectra, which are used to deduce the level energies. The calculated energy for the $2p6d\ ^1F_3^o$ level is 0.2871 eV which is far from the listed value for level 3. The $2p6d\ ^3D_3^o$ level at 0.4706 eV is the only level with the right parity and approximately the right energy. However, the calculated autoionization rate for the $2p6d\ ^3D_3^o$ doubly excited state is very high, see Table III, and it is therefore unlikely that a radiative transition has been observed from this state and, hence, level 3 is most likely also based on some erroneous assignment.

The radiative transition rates and strengths listed are calculated from Eqs. (4) and (3). As seen in Table III, the autoionization rates are for most resonances several orders of magnitude larger than the radiative rates, which means $A^a A^{rad}/(A^a + A^{rad}) \approx A^{rad}$.

The cross section for recombination shown in Fig. 4 is calculated with method 2. Figure 4 thus shows radiative recombination as well as dielectronic recombination. The $1/\varepsilon_e$ dependence of the cross section is clearly seen for the pure radiative contribution (dotted line) as a straight line in log-log scale. For zero relative energy the cross section thus goes to infinity. The recombination rate coefficients, obtained by folding the product of the cross section and the relative electron-ion velocity with a velocity distribution, are however finite, see Sec. V C below. The low-energy recombination cross section is unusually large for F^{6+} due to the low-energy DR resonances. The $J=2$ resonance at 11 meV is easy to recognize in the spectrum. The $J=1$ resonance at 7 meV can, on the other hand, not be distinguished from the radiative background (we separate it as the bold line in Fig. 4) and will appear in an experiment as an enhancement of the background.

C. Comparison of theory and experiment

For comparison with experiment, the calculated cross section is folded with an energy distribution corresponding to

TABLE III. Calculated resonance positions, widths, and strengths for the F⁵⁺(2p_{6l_j') resonances. The second column gives the dominating LS term and the extent to which it describes the state. The autoionization rate is denoted with A^a and the radiative rate with A^{rad}.}

	Dom. LS term to %	Resonance position (eV)	Width (eV)	A ^a (nsec ⁻¹)	A ^{rad} (nsec ⁻¹)	Strength (10 ⁻²⁰ eV cm ²)
(2p _{3/2} 6p _{1/2}) ₁	³ P 60%	0.0069	0.0258	39140.74	7.7	415.09 ^a
(2p _{3/2} 6p _{1/2}) ₂	³ P 92%	0.0114	0.0001	139.98	7.0	363.63
(2p _{1/2} 6d _{3/2}) ₂	³ F 79%	0.0519	0.0087	13177.12	7.3	86.97
(2p _{1/2} 6d _{5/2}) ₃	³ F 93%	0.0990	0.0113	17112.59	6.7	58.35
(2p _{3/2} 6p _{3/2}) ₂	¹ D 93%	0.1158	0.0003	486.00	7.8	40.89
(2p _{1/2} 6d _{5/2}) ₂	¹ D 68%	0.1324	0.0039	5911.02	13.2	61.78
(2p _{3/2} 6d _{5/2}) ₄	³ F 100%	0.1683	0.0110	16645.51	4.9	32.18
(2p _{1/2} 6d _{3/2}) ₁	³ D 84%	0.2240	0.0042	6451.87	16.1	26.62
(2p _{3/2} 6d _{3/2}) ₂	³ D 58%	0.2471	0.0073	11119.49	20.8	52.04
(2p _{1/2} 6f _{5/2}) ₃	³ G 57%	0.2628	0.0243	36907.40	6.5	21.57
(2p _{1/2} 6f _{7/2}) ₄	³ F 46%	0.2730	0.0242	36727.22	5.7	23.06
(2p _{1/2} 6f _{7/2}) ₃	³ F 50%	0.2733	0.0010	1545.57	6.1	19.19
(2p _{1/2} 6f _{5/2}) ₂	³ F 86%	0.2796	0.0001	210.35	6.1	13.02
(2p _{3/2} 6d _{5/2}) ₃	¹ F 96%	0.2871	0.0015	2301.39	25.9	77.22
(2p _{1/2} 6g _{7/2}) ₄	³ H 56%	0.3057	0.0187	28458.19	3.6	13.09
(2p _{1/2} 6g _{9/2}) ₅	³ G 45%	0.3064	0.0187	28374.30	3.6	15.95
(2p _{1/2} 6g _{7/2}) ₃	³ G 69%	0.3070	0.0001	146.18	3.7	10.23
(2p _{1/2} 6g _{9/2}) ₄	³ G 38%	0.3071	0.00001	19.63	3.7	11.16
(2p _{1/2} 6h _{9/2}) ₄	³ H 55%	0.3132	0.00005	72.27	2.6	8.80
(2p _{1/2} 6h _{11/2}) ₅	³ G 45%	0.3133	0.00005	81.63	2.6	10.79
(2p _{1/2} 6h _{9/2}) ₅	³ I 60%	0.3151	0.0074	11225.43	2.5	10.72
(2p _{1/2} 6h _{11/2}) ₆	³ H 40%	0.3153	0.0074	11224.63	2.5	12.66
(2p _{3/2} 6d _{5/2}) ₂	³ P 66%	0.3267	0.0175	26607.49	9.4	17.70
(2p _{3/2} 6d _{3/2}) ₁	³ P 86%	0.3408	0.0228	34659.34	18.4	20.07
(2p _{3/2} 6d _{3/2}) ₀	³ P 100%	0.3485	0.0263	39944.49	14.4	5.12
(2p _{3/2} 6p _{3/2}) ₀	¹ S 98%	0.3632	0.1383	210172.77	7.9	2.69
(2p _{3/2} 6f _{5/2}) ₃	³ G 43%	0.3668	0.0189	28642.00	6.4	15.00
(2p _{3/2} 6f _{7/2}) ₄	³ F 52%	0.3734	0.0214	32538.25	6.4	19.01
(2p _{3/2} 6f _{7/2}) ₅	³ G 100%	0.3987	0.0441	66933.83	6.7	22.96
(2p _{3/2} 6g _{7/2}) ₄	³ H 44%	0.4123	0.0149	22574.30	3.8	10.23
(2p _{3/2} 6g _{9/2}) ₅	¹ H 56%	0.4129	0.0150	22739.61	3.8	12.52
(2p _{3/2} 6f _{5/2}) ₄	¹ G 77%	0.4214	0.0463	70396.29	6.7	17.66
(2p _{3/2} 6h _{9/2}) ₅	³ I 40%	0.4257	0.0049	7377.27	2.7	8.61
(2p _{3/2} 6h _{11/2}) ₆	³ H 60%	0.4261	0.0049	7438.08	2.7	10.19
(2p _{3/2} 6h _{9/2}) ₄	³ H 45%	0.4324	0.000004	6.73	2.7	4.98
(2p _{3/2} 6h _{11/2}) ₅	³ G 55%	0.4326	0.00002	23.52	2.7	7.64
(2p _{3/2} 6f _{7/2}) ₃	³ D 83%	0.4331	0.0010	1533.68	6.7	13.28
(2p _{3/2} 6g _{9/2}) ₄	³ F 69%	0.4357	0.0001	118.79	3.9	9.56
(2p _{3/2} 6g _{7/2}) ₃	¹ F 38%	0.4359	0.0002	291.29	3.9	7.64
(2p _{3/2} 6g _{9/2}) ₆	³ H 100%	0.4420	0.0335	50906.41	4.0	14.55
(2p _{3/2} 6g _{7/2}) ₅	³ G 55%	0.4426	0.0336	51004.35	4.0	12.27
(2p _{3/2} 6f _{5/2}) ₂	³ D 69%	0.4454	0.0009	1438.45	6.5	9.01
(2p _{3/2} 6h _{9/2}) ₆	¹ I 54%	0.4467	0.0121	18446.56	2.9	10.44
(2p _{3/2} 6h _{11/2}) ₇	³ I 100%	0.4470	0.0122	18597.81	2.9	12.07
(2p _{3/2} 6h _{9/2}) ₃	³ G 100%	0.4515	0.0001	115.76	2.8	5.31
(2p _{3/2} 6h _{11/2}) ₄	³ G 55%	0.4516	0.0001	127.80	2.8	6.83
(2p _{3/2} 6g _{7/2}) ₂	³ F 100%	0.4658	0.0001	227.60	4.1	5.29
(2p _{3/2} 6g _{9/2}) ₃	³ F 56%	0.4662	0.0003	416.20	4.1	7.62
(2p _{3/2} 6d _{3/2}) ₃	³ D 93%	0.4706	0.0574	87198.06	20.8	38.24
(2p _{3/2} 6f _{5/2}) ₁	³ D 100%	0.4729	0.0012	1865.82	6.8	5.28
(2p _{3/2} 6f _{7/2}) ₂	¹ D 73%	0.4936	0.0008	1218.34	6.7	8.31
(2p _{3/2} 6d _{5/2}) ₁	¹ P 96%	0.5260	0.0248	37749.28	17.3	12.23

^aThe strength given in the table was calculated using Eq. (3); however, this approach is not valid for resonances overlapping the threshold.

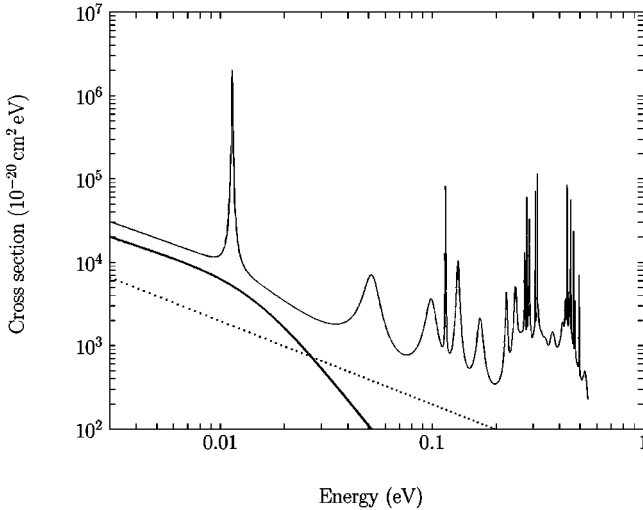


FIG. 4. The calculated cross section for $F^{6+} + e^{-}$ recombining into F^{5+} is plotted against relative energy (thin solid line). The lowest-energy resonance which is narrow and thus distinguishable is situated at 11.4 meV relative energy. The contribution from an even lower-energy resonance, which is broad and overlapping the threshold, is shown separately as the bold line. The pure radiative recombination (RR) is shown by the dotted line.

the respective experimental conditions. Figure 5 contrasts theory with the data from TSR and CRYRING. Generally, the agreement is very good between the data and the calculation, which reproduces all observed spectral features. The lowest narrow resonance is observed experimentally less than 2 meV away from the calculated position of 11.4 meV. Such agreement is found for all individually resolved lines. Single lines are not resolved experimentally in the region between 260 and 520 meV, but here the envelope of the overlapping resonances agrees to within a few meV with the theory, giving confidence that this is true for the underlying individual lines as well. The measured mean absolute rate coefficients between 100 and 550 meV are 11% and 5% below theory for the TSR and CRYRING data, respectively. Hence, both experiments and theory are in mutual agreement based on our estimated experimental uncertainty for absolute rate measurements.

The broad resonance at 7 meV is of particular interest, since its distance from the threshold is less than its computed half-width of 13 meV. As mentioned above, the significant presence of radiative recombination at low energy prevents us from truly resolving this line. However, its presence can be seen unambiguously in the data. In the right graph of Fig. 5 (a) the computed shape of this resonance is indicated by the dashed line. Below ≈ 7 meV strength from this line is required to account for the observed rate. Furthermore, the rate seen in the depression around 20 meV cannot be explained by radiative recombination and tails from resonances at higher energy alone. Again, strength from this additional broad resonance is needed, and the data are compatible with the predicted position, width, and strength. It is unfortunate that the behavior of this peak cannot be studied experimentally very close to threshold (≈ 2 meV), since in this energy

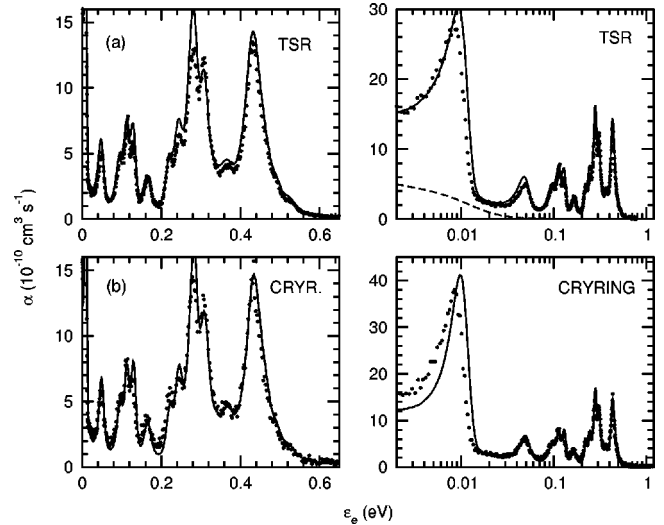


FIG. 5. Comparison between theory (solid line) and the TSR (a) and CRYRING (b) experiments (data points) with no scaling between theory and experiment. The plots on the right show the same data on a logarithmic scale to emphasize the low-energy resonances. The contribution of the broad resonance at $\epsilon_e = 7$ meV (dashed line) is shown separately in the right upper graph. The difference in peak heights between (a) and (b) stems from the difference in kT_{\perp} for the two storage rings. The experimentally derived cross sections differ by only 6%, well inside the estimated experimental uncertainty.

domain merged beam experiments observe a rate enhancement that is so far not well understood [31].

It is interesting to see how the spectrum would look in a purely nonrelativistic description. In this case, the states $1s^2 2pn\ell L (L = \ell)$ cannot autoionize, and correspondingly no recombination occurs, either. Figure 6 demonstrates that such a description is totally inadequate.

It should be noted that Mitnik *et al.* [41] also presented theoretical recombination spectra for F^{6+} recently. They ob-

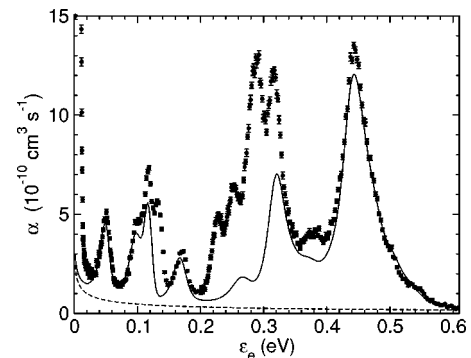


FIG. 6. Comparison between the data (TSR) and theory, if only nonrelativistically autoionizing states are considered [$1s^2 2pn\ell L (L \neq \ell)$, where L is given by the dominant LS term in Table III], as shown by the solid line (including radiative recombination, which is also shown separately by the dashed line). Note that the narrow resonance at 11 meV is missing. The theoretical spectrum was assembled from Lorentzians as listed in Table III, leaving out the terms $1s^2 2pn\ell L (L = \ell)$.

tained their results from distorted-wave as well as R -matrix calculations. Their resonance positions do not agree well with the experimental and theoretical data presented here. For example, the narrow resonance at 11 meV appears at ≈ 40 meV in their spectra. Still, from a measurement a decade ago [4] it would have been difficult to tell which one of the calculations is more reliable. This indicates how important the improved resolution and accuracy of the merged-beam experiments are for testing the accuracy of different calculations.

From an experimental point of view, the agreement between the data collected at TSR and CRYRING shows impressively that merged-beam experiments in storage-ring electron coolers can yield reliable spectra all the way down to relative electron-ion energies of at least kT_{\perp} . As described in Sec. IV, technical details such as the methods used for scanning the electron beam, detection, energy calibration, etc., differ significantly between the two storage rings, yet the results are virtually identical.

VI. CONCLUSIONS

We present theoretical and experimental recombination spectra for F^{6+} in the energy region of the $1s^2 2p 6l$ resonances, i.e., in the region 0–0.6 eV. The theoretical data include energy positions, natural widths, autoionization rates,

radiative rates, and DR strengths for the 52 available doubly excited states. Two slightly different methods were used to obtain the theoretical results, and they gave consistent results.

Recombination spectra obtained independently from storage-ring experiments at TSR in Heidelberg and at CRYRING in Stockholm are compared with theory and the agreement is found to be very good. Calculated line positions agree with experiment to within 2 meV, and the computed rate coefficients are experimentally confirmed to within 5%–10%, which is well inside the experimental errors. Moreover, the two experiments are in excellent agreement with each other, which demonstrates that storage-ring experiments are able to determine precise recombination rates and resonance energies for collision energies all the way down to a few meV.

ACKNOWLEDGMENTS

Financial support for this research was received from the Swedish Science Research Council (VR). M.T. is grateful to the Swedish Royal Academy of Science for support. The Giessen group gratefully acknowledges support by Deutsche Forschungsgemeinschaft and by Bundesministerium für Bildung und Forschung.

-
- [1] R. Brooks, R. Datla, and H. Griem, *Phys. Rev. Lett.* **41**, 107 (1978).
 - [2] C. Breton, C. D. Michelis, M. Finkenthal, and M. Mattioli, *Phys. Rev. Lett.* **41**, 110 (1978).
 - [3] P. F. Dittner *et al.*, *Phys. Rev. A* **35**, 3668 (1987).
 - [4] L. Andersen *et al.*, *Phys. Rev. A* **45**, 6332 (1992).
 - [5] W. Zong *et al.*, *Phys. Rev. A* **56**, 386 (1997).
 - [6] W. Zong *et al.*, *J. Phys. B* **31**, 3729 (1998).
 - [7] E. Lindroth, *Hyperfine Interact.* **114**, 219 (1998).
 - [8] S. Mannervik *et al.*, *Phys. Rev. Lett.* **81**, 313 (1998).
 - [9] P. Glans *et al.*, *Phys. Rev. A* **64**, 043609 (2001).
 - [10] S. Salomonson and P. Öster, *Phys. Rev. A* **40**, 5559 (1989).
 - [11] S. Salomonson and P. Öster, *Phys. Rev. A* **40**, 5548 (1989).
 - [12] S. Salomonson and P. Öster, *Phys. Rev. A* **41**, 4670 (1990).
 - [13] E. Lindroth and J. Hvarfner, *Phys. Rev. A* **45**, 2771 (1991).
 - [14] E. Lindroth, *Phys. Rev. A* **49**, 4473 (1994).
 - [15] D. R. DeWitt *et al.*, *J. Phys. B* **28**, L147 (1995).
 - [16] For an account of the early contributions to the complex rotation method see the whole No. 4 issue of *Int. J. Quantum Chem.* **14** (1978).
 - [17] Y. K. Ho, *Phys. Rev. A* **23**, 2137 (1981).
 - [18] K. T. Chung and B. F. Davis, *Phys. Rev. A* **26**, 3278 (1982).
 - [19] I. Lindgren, *J. Phys. B* **7**, 2441 (1974).
 - [20] E. Lindroth and A.-M. Mårtensson-Pendrill, *Phys. Rev. A* **53**, 3151 (1996).
 - [21] A.-M. Mårtensson-Pendrill *et al.*, *Phys. Rev. A* **51**, 3630 (1995).
 - [22] H. Feshbach, *Ann. Phys. (N.Y.)* **5**, 357 (1958).
 - [23] C. Bloch, *Nucl. Phys.* **6**, 329 (1958).
 - [24] T. Pacher, L. Cederbaum, and H. Köppel, *J. Chem. Phys.* **89**, 7367 (1988).
 - [25] E. Lindroth, *Phys. Rev. A* **52**, 2737 (1995).
 - [26] T. N. Rescigno and V. McKoy, *Phys. Rev. A* **12**, 522 (1975).
 - [27] M. Griesser *et al.*, in *Proceedings of the 19th International Symposium on Cooler Rings and Their Applications, Tokyo, 1990*, edited by T. Katayama and A. Noda (World Scientific, Singapore, 1991), p. 190.
 - [28] G. Miersch *et al.*, *Nucl. Instrum. Methods Phys. Res. A* **369**, 277 (1996).
 - [29] H. Danared *et al.*, *Phys. Rev. Lett.* **72**, 3775 (1994).
 - [30] S. Pastuszka *et al.*, *Nucl. Instrum. Methods Phys. Res. A* **369**, 11 (1996).
 - [31] G. Gwinner *et al.*, *Phys. Rev. Lett.* **84**, 4822 (2000).
 - [32] R. Kelly, *J. Phys. Chem. Ref. Data* **16**, 135 (1987).
 - [33] S. Schippers *et al.*, *Astrophys. J.* **555**, 51027 (2001).
 - [34] A. Lampert *et al.*, *Phys. Rev. A* **53**, 1413 (1996).
 - [35] P. Glans *et al.*, *Nucl. Instrum. Methods Phys. Res. B* **154**, 97 (1999).
 - [36] E. Lindroth *et al.*, *Phys. Rev. Lett.* **86**, 5027 (2001).
 - [37] W. R. Johnson, S. A. Blundell, and J. Sapirstein, *Phys. Rev. A* **37**, 2764 (1988).
 - [38] W. R. Johnson and G. Soff, *At. Data Nucl. Data Tables* **33**, 405 (1985).
 - [39] S. A. Blundell, *Phys. Rev. A* **46**, 3762 (1992).
 - [40] NIST *Atomic Spectra Database* (WWW published at http://physics.nist.gov/cgi-bin/AtData/main_asd).
 - [41] D. Mitnik, M. Pindzola, and N. Badnell, *Phys. Rev. A* **59**, 3592 (1999).